JMEPEG
https://doi.org/10.1007/s11665-024-09352-3

©ASM International
1059-9495/$19.00

ORIGINAL RESEARCH ARTICLE

Effects of Trace La on the Aging Properties of the Cu-Ti-Zr Alloys

Nengneng Wang, Meng Zhou, Baohong Tian, Jin Zou, Ke Jing, Haoyan Hu, Yi Zhang, Qian Bai, Caijiao Tian, Xu Li, and Alex A. Volinsky

Submitted: 17 November 2023 / Revised: 10 January 2024 / Accepted: 5 February 2024

Cu-2Ti-0.3Zr and Cu-2Ti-0.3Zr-0.2La alloys were prepared by vacuum melting, and their mechanical properties and conductivity were measured after aging treatment. Both alloys were aged at 450 °C for 30 min to obtain optimum properties, and the microhardness of the Cu-Ti-Zr-La alloy increased by 8.5% and the strength by 5% compared to the Cu-Ti-Zr alloy. Characterization of the alloys by EBSD revealed that the addition of La inhibits grain growth, refines the grains and enhances the texture. The Cu_4Ti phase precipitated during the Cu-Ti-Zr alloy's aging process, and the Cu_5Zr phase precipitated after La was added. It was found by analyzing the strengthening mechanisms of the Cu-Ti-Zr-La alloy that precipitation strengthening significantly contributes to the alloy strength.

Keywords Cu-Ti-Zr and Cu-Ti-Zr-La alloys, mechanical properties, microstructure, strengthening mechanisms

1. Introduction

Due to their excellent electrical, thermal, and elastic modulus, copper alloys have found extensive application in the field of electrically conductive materials and devices (Ref 1-5). Higher standards have been set in recent years for the conductivity and strength of materials based on copper (Ref 6-9). Cu-Be alloy is a typical high-strength and high elasticity medium conductivity copper alloy, but the production cost of Be is high, and toxic substances are generated during the melting process (Ref 10-13). Therefore, developing substitute materials for Cu-Be alloys is crucial. By adding alloying elements and refining process parameters, Cu-Ti alloys can get mechanical qualities that are similar to Cu-Be alloys; however, the electrical conductivity may be marginally decreased (Ref 14).

In numerous studies, the properties of Cu-Ti alloys have been improved by adding alloying elements, including Mg (Ref 15, 16), Cr (Ref 17-19), Zr (Ref 20), Al (Ref 21, 22) and Co (Ref 23-25), as trace elements. Markandeya et al. (Ref 26-28) found that the addition of the element Cr precipitated the Cr_2Ti phase, which will enhance the mechanical characteristics of Cu-3Ti-Cr and Cu-4Ti-Cr alloys. Nevertheless, Ti and Cr dissolve in the copper matrix, which negatively impacts the alloy's electrical conductivity. Konno et al. (Ref 29) demonstrated that the early aging stage of Cu-Ti-Al alloys can be prevented from experiencing spinodal decomposition by adding Al. An $AlCu_2Ti$ phase is formed, which contributes to the copper matrix's purification and increased electrical conductivity. Wang et al. (Ref 30) added 0.4 wt.% Co to the Cu-3.6Ti alloy and observed significant improvements in the aging peak hardness of Cu-3.6Ti-0.4Co alloy through cold rolling and aging. Under 75% cold deformation, the peak microhardness could reach 383 HV when aged at 450 °C for 1 h. Cao et al. 31 discovered that 0.1 wt.% Zr can inhibit Cu_4Ti from becoming Cu_3Ti, increasing the Cu-Ti-Zr alloy's heat resistance. Markandeya et al. (Ref 32) reported that the tensile strength of Cu-3Ti-0.1Zr and Cu-4Ti-0.1Zr alloys at peak aging reached 802 MPa and 846 MPa, respectively. Additionally, no discontinuous precipitation was observed in the alloy during over-aging.

The addition of Ti leads to a lower electrical conductivity in Cu-Ti alloys. Therefore, to maintain the electrical conductivity of the alloy, a lower Ti content (2 wt.%) was chosen in this study. Simultaneously, trace amounts of Zr were added to achieve precipitation strengthening, which has a negligible effect on the electrical resistivity of the alloy. Furthermore, La (0.2 wt.%) was added to the Cu-2Ti-0.3Zr alloy to investigate its influence on the alloy properties. Analysis of the microstructure, precipitated phases, and strengthening mechanisms after age was conducted on Cu-2Ti-0.3Zr (Cu-Ti-Zr) and Cu-2Ti-0.3Zr-0.2La (Cu-Ti-Zr-La) alloys using cold rolling and aging tests. The purpose is to create high-strength copper alloys that meet the demands of the application by combining cold rolling and aging treatments.

Nengneng Wang, Meng Zhou, Baohong Tian, Ke Jing, Haoyan Hu, Yi Zhang, and **Caijiao Tian**, School of Materials Science and Engineering, Henan University of Science and Technology, Provincial and Ministerial Co-construction of Collaborative Innovation Center for Non-ferrous Metals New Materials and Advanced Processing Technology, Luoyang 471023, People's Republic of China; **Jin Zou**, Jiangxi Key Laboratory for Advanced Copper and Tungsten Materials, Jiangxi Academic of Sciences, Nanchang 330096, China; **Qian Bai**, Medical Research Center, The Second Affiliated Hospital of Zhengzhou University, Zhengzhou 450014, People's Republic of China; **Xu Li**, Center for Advanced Measurement Science, National Institute of Metrology, Beijing 100029, People's Republic of China; and **Alex A. Volinsky**, Department of Mechanical Engineering, University of South Florida, 4202 E. Fowler Ave. ENG 030, Tampa 33620. Contact e-mails: zhoumeng0902@126.com, niatzou@126.com, zhshgu436@163.com, and baiqian@zzu.edu.cn.

Journal of Materials Engineering and Performance

2. Materials and Methods

Copper cathode No. 1 Cu-CATH-1, 99% Ti titanium sponge, Cu-10% Zr, and Cu-10% La intermediate alloys were the materials chosen for the melting of Cu-Ti-Zr and Cu-Ti-Zr-La alloys. Divide the prepared raw materials into small pieces and put them into a ZG-0.01-40-4 intermediate frequency vacuum induction furnace for melting. During the melting process, argon gas was passed to prevent the alloy from oxidizing. The melting temperature was controlled between 1.150 and 1.250 °C for casting. The casting with Φ80 mm × 150 mm size was finally cooled to room temperature. Table 1 lists the two alloys' measured compositions.

Following demolding, the alloy was first homogenized for 1 h at 880 °C in an RJX45-9 box furnace. Using a C41-750 air hammer, the ingot was then hot forged into Φ40 × 230 mm bars. The alloy was then subjected to solution and aging treatments in a KSS-1200 tubular resistance furnace with argon gas as a protective atmosphere. The alloy underwent a one-hour solution treatment at 900 °C before being quenched in water. After being cold-deformed to 60%, the samples were aged. 400-550 °C was the aging temperature, while 10-480 min was the aging duration. The aging technological process of the alloy is shown in Fig. 1.

Vickers hardness (GB/T 4340.1-1999) was employed to characterize the alloy's mechanical characteristics. The HVS-1000 microhardness tester was used to test the microhardness of the alloys in their various states. The load was 0.3 kgf, and the holding period was 15 s. Each specimen's hardness was measured in six distinct zones to reduce error; the average value was then determined by subtracting the maximum and minimum readings. The conductivity of Cu-Ti-Zr and Cu-Ti-Zr-La alloys in various states was measured using a Sigma 2008B digital conductivity meter. The conductivity meter needs to be calibrated using a standard sample before the test, and after calibration, five sets of positive and negative measurements are made on each specimen, and the specimen's conductivity is determined by averaging the measurement findings.

After aging the two alloys' microstructures were analyzed using electron back scatter diffraction (EBSD). The EBSD specimens were prepared by first rough grinding the specimens using different types of sandpaper, performing fine grinding and polishing on a polishing machine, and finally electrolytic polishing when the specimen surface was smooth. During electrolytic polishing, the DC-regulated power supply's voltage was adjusted to roughly 5 V, and its current was set to its maximum value. Using an electrolytic solution composed of 50% anhydrous phosphoric acid and 50% anhydrous alcohol. The samples were electrolytically polished for approximately one minute. After the specimens were prepared, they were viewed and analyzed on a JSM-7800F with a step size and voltage of 2.5 μm and 20 kV, respectively.

Table 1 Composition of alloys

	Alloy element, wt.%			
Alloy	**Ti**	**Zr**	**La**	**Cu**
Cu-2Ti-0.3Zr	2.01	0.255	…	Bal.
Cu-2Ti-0.3Zr-0.2La	1.94	0.301	0.213	Bal.

Characterizing the microscopic morphology of the alloy in the peak aging state using transmission electron microscopy (TEM), which observes the types and locations of precipitated phases in the alloys at their peak-aging stage. The TEM specimens were prepared by first sanding the thickness of the specimens to less than 50 μm, then punching out 3 mm diameter disks, and finally thinning the disks using a Gatan 691 ion thinning instrument. After completing the preparation of TEM specimens, the samples were analyzed using a JEM-2100F transmission electron microscope operated at 200 kV with 0.19 nm resolution.

3. Results

3.1 Mechanical Properties and Conductivity

Figure 2 illustrates the micro-hardness, conductivity, and tensile strength of two alloys in different states, which were obtained in order to explore the impacts of La on the post-solution aging precipitation properties of Cu-Ti-Zr alloys. Three stages of aging may be differentiated from Fig. 2(a) and (d), which are under-aging, peak-aging and over-aging (Ref 33, 34). In Fig. 2(a), for instance, the Cu-Ti-Zr alloy ages at 450 °C, and as the aging time increases from 0 to 20 min, there is a noticeable rise in micro-hardness. This is the stage of under-aging. At this time after the solution treatment, the alloy is in a supersaturated state, and the precipitation phase will precipitate rapidly. It then enters the stage of peak aging, by now, the micro-hardness has reached its maximum value of 272 HV, and the aging time is 30 min. The over-aging stage is indicated by a decrease in micro-hardness after 60 min of aging. The Cu-Ti-Zr alloys' peak micro-hardness likewise increases and thereafter declines at varying aging temperatures. At 400 °C, it was 264 HV, then at 450 °C, it was 272 HV, and at 550 °C, it dropped to 235 HV.

Figure 2(d) depicts the micro-hardness variation of Cu-Ti-Zr-La alloys under various aging situations. Similar to Cu-Ti-Zr alloys, the micro-hardness rises gradually during under-aging until it reaches its maximum. Following the peak-aging, the micro-hardness progressively declines over time to enter the over-aging stage. Moreover, at various aging temperatures, the alloys' peak micro-hardness rises and then falls. Using the aging temperature of the Cu-Ti-Zr-La alloy at 450 °C in Fig. 2(d) as an example, the Cu-Ti-Zr-La alloy's micro-hardness increased from 189 HV in the cold-rolled state to 295 HV at peak-aging during the aging process, and then, it decreased to 252 HV at the aging time of 480 min. The micro-hardness of the Cu-Ti-Zr-La alloy reached its maximum after 30 min of aging at 450 °C. At this time, it is 295 HV.

The solute atoms (Ti, Zr, and La) dissolved in the supersaturated solid solution intensify the effects of electron scattering, resulting in alloys having reduced conductivity. As aging time rises, the Cu-Ti-Zr alloy's conductivity varies, according to Fig. 2(b). As a result of second-phase precipitation and the supersaturated solid solution breakdown, which reduces the solute atom in the Cu matrix and lowers lattice distortion, the conductivity increases quickly with aging time. However, it continues to increase the aging time and the reduced second-phase precipitation rate. At this point, the conductivity did not change significantly and stabilized. The Cu-Ti-Zr-La alloy conductivity varies with aging temperature and aging time, as

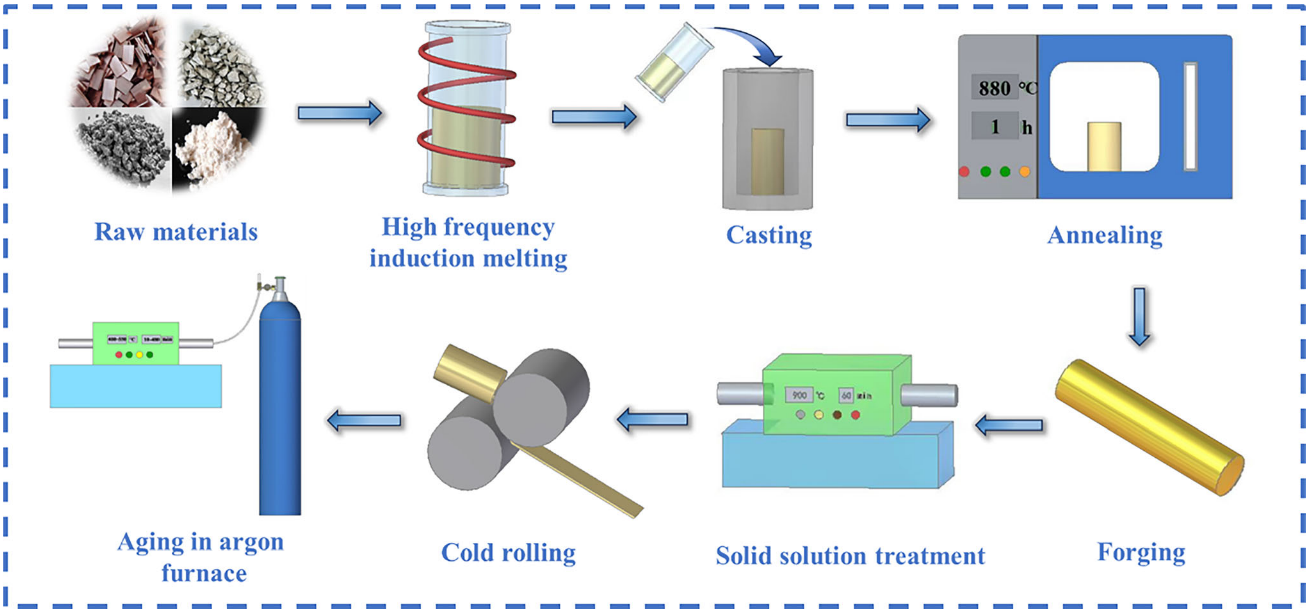

Fig. 1 Flow chart of the aging experiment of alloys

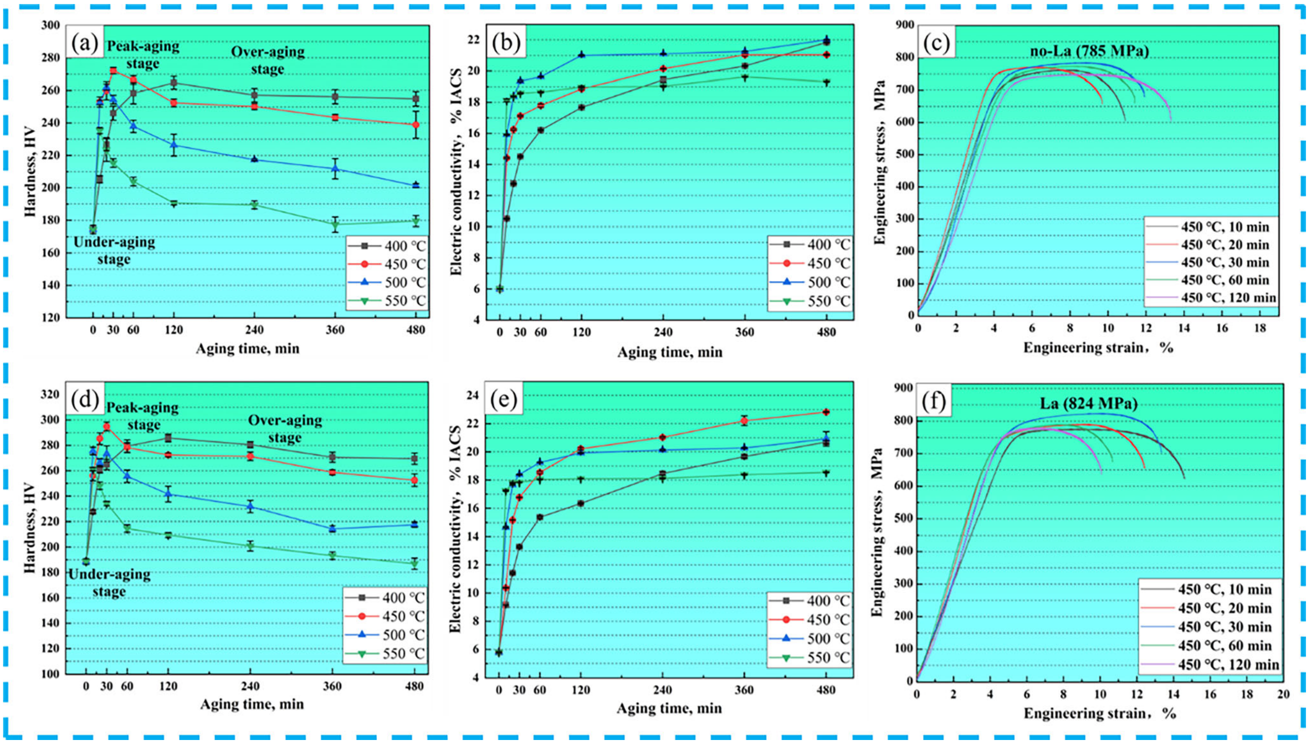

Fig. 2 (a, d) Microhardness, (b, e) electrical conductivity, and (c, f) engineering tensile stress–strain curves of the Cu-Ti-Zr and Cu-Ti-Zr-La alloys after 60% deformation: (a-c) Cu-Ti-Zr, (d-f) Cu-Ti-Zr-La alloys

illustrated in Fig. 2(e). The trend of change is in line with that of the Cu-Ti-Zr alloy, in which electrical conductivity rises more quickly during the under-aging phase before increasing more slowly and eventually tending to level off gradually. In Fig. 2(e), the conductivity of the Cu-Ti-Zr-La alloy increases during the 450 °C aging, from 5.8% IACS in the cold-rolling state to 22.7% IACS after aging for 480 min.

Tensile tests were performed on samples of two alloys aged at 450 °C for 10-120 min, and Fig. 2(c) and (f) displays the tensile strength. The tensile strength of Cu-Ti-Zr alloy can be obtained from Fig. 2(c), which increases from 763 MPa at 10 min aging time to 785 MPa at peak aging and decreases to 751 MPa at 120 min aging time. Similarly, the Cu-Ti-Zr-La alloy rises from 777 MPa at the beginning of aging to 824 MPa at the peak aging and then falls to 780 MPa as the aging time is prolonged to 120 min. The changes in the alloy's tensile strength are in line with the micro-hardness and are rising first and then decreasing. After 30 min of aging at 450 °C, the Cu-

Ti-Zr and Cu-Ti-Zr-La alloys displayed the highest microhardness values. The maximum tensile strengths of 824 MPa and 785 MPa with elongations of 13.5% and 12.1% were obtained for the two alloys by conducting tensile tests under this aging condition.

In summary, aging at 450 °C for 30 min is the optimum aging process parameters for Cu-Ti-Zr and Cu-Ti-Zr-La alloys. The alloy's strength and microhardness are increased by the addition of La, but its electrical conductivity is marginally poorer. Overall, the Cu-Ti-Zr-La alloy has better overall performance.

Fracture of alloys is a dynamic process and the fracture mode of alloys can be determined by fracture morphology (Ref 35-37). The fracture micro-morphology of two alloys aged at 450 °C is shown in Fig. 3. A large number of round or elliptical dimples can be observed in Fig. 3 (pointed by yellow arrows), which are obvious plastic fracture characteristics, and there are small dimples clustered around the large dimples, indicating that the specimen was plastically deformed before fracture. Metals tensile fracture usually undergoes nucleation, growth, and aggregation of micropores (Ref 38), and a large number of equiaxial dimples and sharp tear marks can be seen in the fracture morphology of Fig. 3. It can be deduced that the growth and aggregation of micropores caused the fracture of the Cu-Ti-Zr and Cu-Ti-Zr-La specimens. The undulation of the fracture varies sharply along the position of the bright edge line (indicated by the white arrow), and the change in the undulation of the fracture height predicts localized crack deflection (Ref 39). The size and number of dimples vary at different aging times, and the larger and deeper the dimple, the better plasticity is (Ref 40). Cu-Ti-Zr and Cu-Ti-Zr-La alloys have excellent strength during peak-aging, and observation of the fracture morphology of their tensile specimens in Fig. 3(c) and (g) combined with the elongation obtained from their tensile tests shows that a well-integrated combination of strong plasticity is obtained for the two alloys.

3.2 EBSD Analysis

To explore how La addition impacts the microstructure and texture of aged Cu-Ti-Zr-La alloys, EBSD was used to characterize samples of two alloys that had been aged at 450 °C for 30 and 120 min, respectively. The grain size distribution and EBSD diagram of the Cu-Ti-Zr alloy aged at 450 °C for 30 min are displayed in Fig. 4(a). Numerous recrystallized grains are visible on the EBSD graph, with an average grain size of 78 μm and a 72.2% percentage of grains smaller than 100 μm. Figure 4(b) shows that when the time is extended to 120 min, the grain size increases and recrystallized grain grows. At this point, only 37.5% of the grains are smaller than 100 μm, and the average grain size has reached 196.4 μm, a 152% increase in average grain size when compared to 30 min of aging. Average grain size increases as aging time increases because the alloy's recrystallized grains possess more time for growth and nucleation.

The Cu-Ti-Zr-La alloy's EBSD map and grain size map after 30 and 120 min of aging at 450 °C are displayed in Fig. 4(c) and (d). An average grain growth of 37% (from 30 to 41.2 μm) can be observed with increasing time. Due to the impacts of cold deformation, some twins can be seen in Fig. 4(d). Comparing Fig. 4(a), (b), (c) and (d) reveal that while the two alloys' grains have the same tendency to grow, the Cu-Ti-Zr-La alloy's average grain increases by only 37%, and the tendency of grain growth decreases. The results demonstrate that adding the element La can inhibit grain growth, that there is a noticeable effect of grain refinement, and that fine grain strengthening increases the micro-hardness and strength of the Cu-Ti-Zr-La alloy. The strength and hardness of the Cu-Ti-Zr-La alloys are higher than the Cu-Ti-Zr alloys when aged at 450 °C for 30 min and 120 min, while the electrical conductivity is slightly reduced due to the grain refinement, which increases the area of grain boundaries. These results are consistent with the aging strengthening results of the two alloys.

The orientation angle distribution and kernel average misorientation maps (KAM) of the alloys are shown in Fig. 6. The alloy characteristics are influenced by the dislocation density ρ (Ref 41), which may be computed using the KAM data acquired:

$$\rho = 2\theta/\mu b \tag{Eq 1}$$

Here ρ is the dislocation density (m^{-2}), θ is the difference in average local orientation (rad), μ is the step size (2.5 μm), and b is the Burgers vector (0.225 nm).

The dislocation density of the alloy aged for 30 and 120 min, when combined with the computations in Fig. 5, the dislocation densities for the Cu-Ti-Zr alloy are 3.15×10^{14} m^{-2} and 2.70×10^{14} m^{-2}, and for the Cu-Ti-Zr-La alloy, they

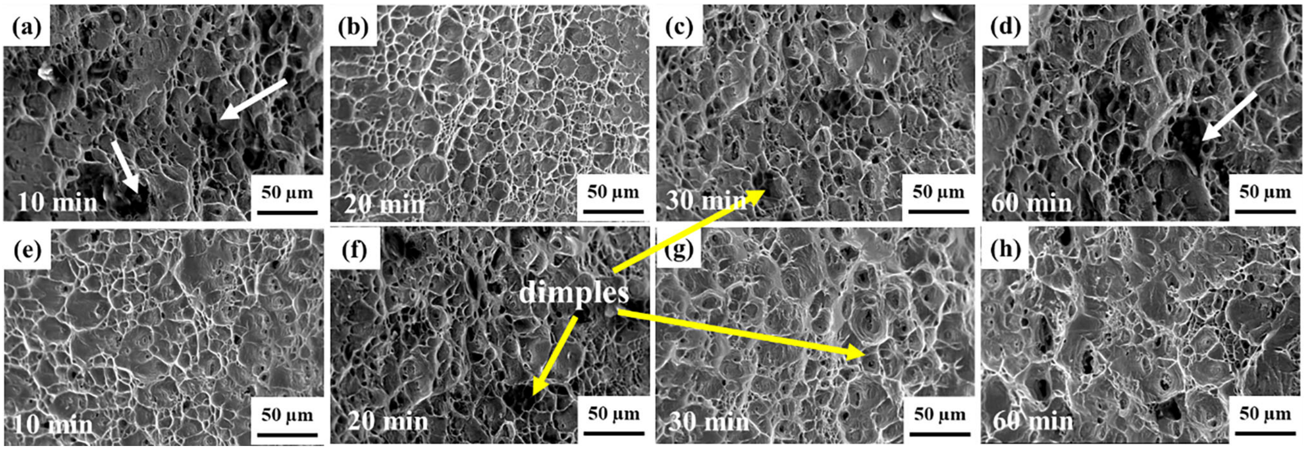

Fig. 3 Cu-Ti-Zr and Cu-Ti-Zr-La alloys' scanning fracture morphology at 60% deformation and various aging durations (10-60 min) at 450 °C: (a-d) Cu-Ti-Zr and (e-h) Cu-Ti-Zr-La alloys

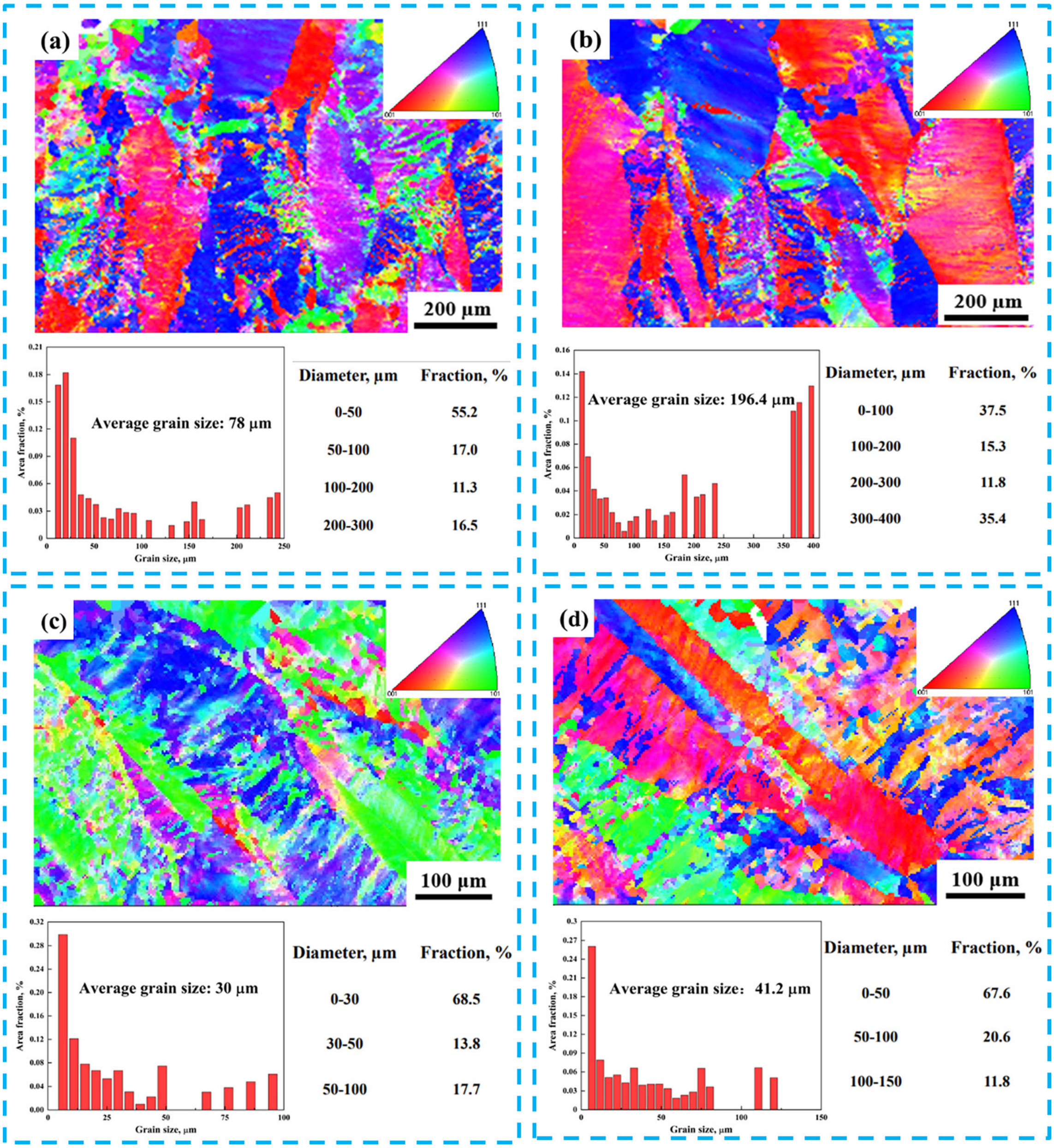

Diameter, μm	Fraction, %
0-50	55.2
50-100	17.0
100-200	11.3
200-300	16.5

Diameter, μm	Fraction, %
0-100	37.5
100-200	15.3
200-300	11.8
300-400	35.4

Diameter, μm	Fraction, %
0-30	68.5
30-50	13.8
50-100	17.7

Diameter, μm	Fraction, %
0-50	67.6
50-100	20.6
100-150	11.8

Fig. 4 Maps of EBSD and grain sizes of Cu-Ti-Zr (a, b) and Cu-Ti-Zr-La (c, d) alloys aged at 450 °C for: (a, c) 30 min, (b, d) 120 mi

are 2.58×10^{14} m^{-2} and 2.66×10^{14} m^{-2}, respectively. Compared to Cu-Ti-Zr alloys, the dislocation density of Cu-Ti-Zr-La alloys is lower, indicating that more dislocations are consumed in the Cu-Ti-Zr-La alloys during aging, which can provide more energy for recrystallization, and promote recrystallization. The fine grains generated in the recrystallization process enhance the crystal strengthening effect, as shown macroscopically in the increase in alloy hardness and strength. Hence, Cu-Ti-Zr-La alloys have higher hardness and strength than Cu-Ti-Zr alloys. The increase in grain boundary mobility will accelerate the generation of recrystallized fine grains. The formation of tiny grains is hindered when the orientation angle is small because it causes the grain boundary to migrate slowly. The production of small grains during the recrystallization process is encouraged to a greater extent by larger values of the large-angle grain boundary. As demonstrated in Fig. 5(f), (h), (b) and (d), the proportion of large-angle grain boundaries in the Cu-Ti-Zr alloys is 20.4% and 17.2%, respectively, which is lower than that of the Cu-Ti-Zr-La alloys (21.3% and 24.6%, respectively) under the same aging conditions. It is further demonstrated that the addition of La element promotes the occurrence of recrystallization.

With Cu-Ti-Zr and Cu-Ti-Zr-La alloys aged at 450 °C for 30 and 120 min, respectively, pole figures and inverse pole figures are plotted in Fig. 6 to explore the textural change in Cu-Ti-Zr-La alloys with the addition of La. As shown in Fig. 6(a), (c), (e) and (g), the Cu-Ti-Zr alloy's maximum texture strength after 30 min of aging is 5.897, and after 120 min, it drops to 5.279. Under the same aging conditions, they are all lower than Cu-Ti-Zr-La alloys (7.534 and 5.316). Similarly, the same change rule can be found in the inverse pole figures. Indicating that the addition of La can increase the maximum texture strength of the alloys and inhibit the growth of the recrystallization grain. Its adjacent grains are oriented in the

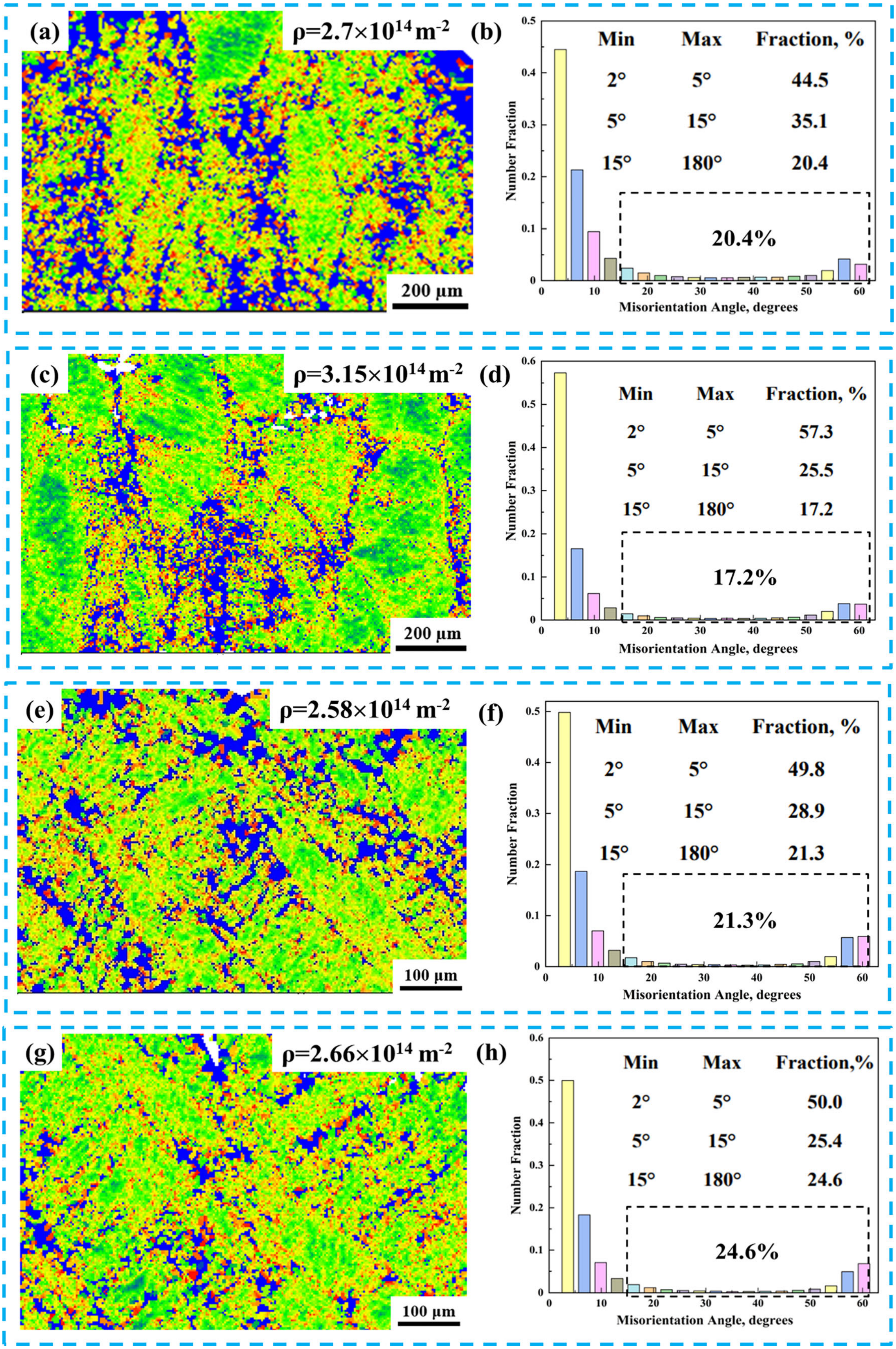

Fig. 5 (a, c, e, g) KAM maps and (b, d, f, h) orientation angle distribution of (a-d) Cu-Ti-Zr alloys and (e-h) Cu-Ti-Zr-La alloys aged at 450 °C for (a, b, e, f) 30 min and (c, d, g, h) 120 min

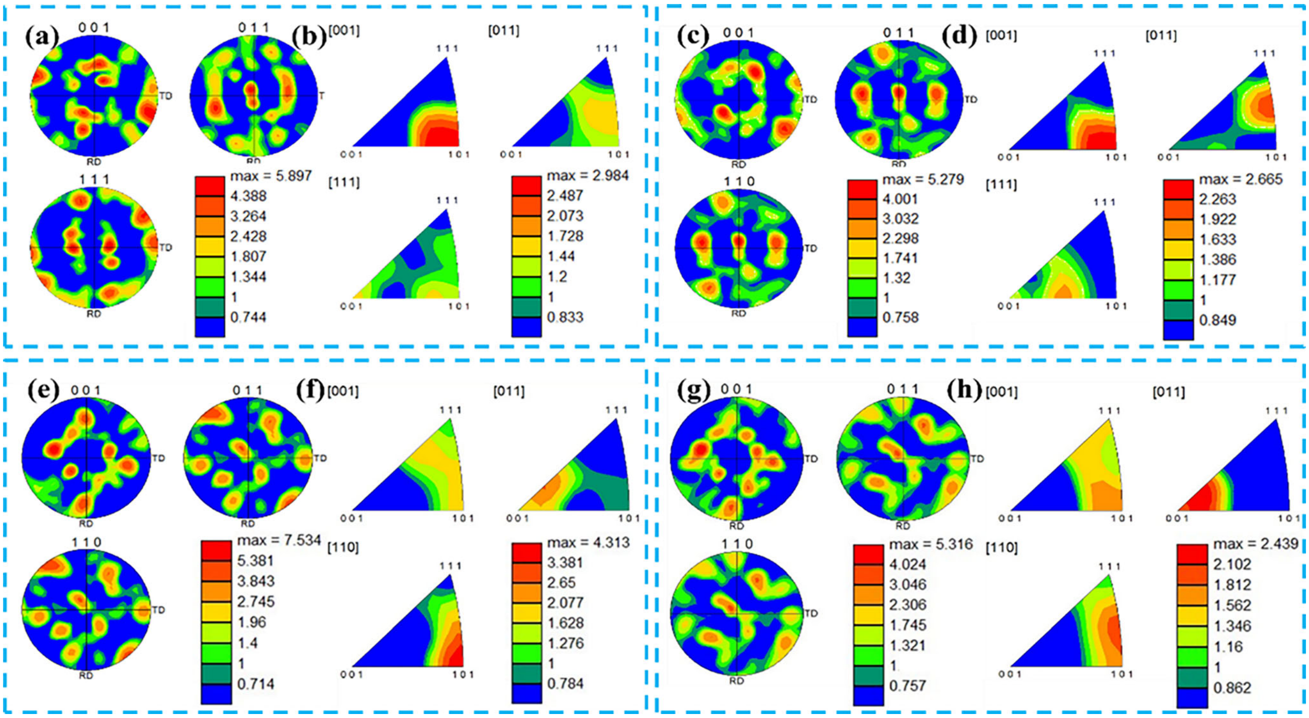

Fig. 6 Pole figures (a, c, e, g) and inverse pole figures (b, d, f, h) of Cu-Ti-Zr alloys (a-d) and Cu-Ti-Zr-La (e-h) alloys aged at 450 °C for 30 min (a, b, e, f) and 120 min (c, d, g, h)

same direction, which leads to a decrease in interfacial energy, a decrease in the driving force for the movement of grain boundaries, and difficulties in grain growth, thus playing a role in refining the grains.

The texture and texture percentages of the two alloys aged for 30 and 120 min at 450 °C are displayed in Fig. 7. Figure 7(a) and (b) shows the distribution of the textures in Cu-Ti-Zr-La alloys. The volume fractions of the corresponding texture of the Cu-Ti-Zr alloy aged for 30 min can be obtained from Fig. 7(c), and the proportions of each texture decreased as the aging was extended to 120 min. Similarly, as the aging time increases in Fig. 7(d), the volume percentage of the Cu-Ti-Zr-La alloy texture falls slightly. A comparison of the two alloys shows that the Cu-Ti-Zr alloys show a decrease in the proportion of the dominant Brass, S, and Cubic textures, as well as a slight decrease in the intensity of the textures. In addition, the main texture of the alloys changed significantly. The Cu-Ti-Zr alloy's primary texture is Brass texture when aged for 30 min, whereas the main texture is Goss texture when aged for 120 min. After 30 min of aging, the Cu-Ti-Zr-La alloy's primary texture is Brass and S texture; after 120 min, the primary textures are Goss, Brass, and S texture. This has a tight connection to the metals' characteristics (Ref 42, 43). Because Cu-Ti-Zr-La alloys contain a higher percentage of Brass, S, and Cube texture, they have better characteristics than Cu-Ti-Zr alloys.

3.3 TEM Analysis

The Cu-Ti-Zr alloy's TEM microstructure after 30 min of aging at 450 °C is displayed in Fig. 8. The bright-field images in Fig. 8(a) and (b) show that the copper matrix contains an abundance of precipitated phases, which can strengthen the matrix. Additionally, the precipitated phases reduce dot aberration in the Cu matrix, which lessens the effects of electron scattering and increases electrical conductivity. Many dislocations are concentrated around the precipitated phase, and the precipitated phase's pinning effect prevents the dislocations from moving, which leads to the dislocations becoming tangled and piling up. In order to determine the type of precipitated phase, the obtained HRTEM images were analyzed as shown in Fig. 8(c). Fast Fourier transform (FFT) was performed on it, diffraction spots were obtained and calibrated, and the precipitated phase was found to be Cu$_4$Ti. The nanoscale precipitated phase's crystallographic band axis was determined to be $[151]_{Cu4Ti}$. The crystal spacing of $(\bar{1}1\bar{4})_{Cu4Ti}$ was measured to be 0.225 nm, $(01\bar{5})_{Cu4Ti}$ was measured to be 0.222 nm, and $(\bar{1}01)_{Cu4Ti}$ was measured to be 0.428 nm. Figure 8(d) shows the diffraction spots on the Cu matrix (obtained by selecting the white part of the BF image for diffraction), and its crystallographic axis was obtained as $[111]_{Cu}$, and the crystal plane spacing was measured to be 0.128 nm for $(02\bar{2})_{Cu}$, 0.128 nm for $(\bar{2}02)_{Cu}$, and 0.128 nm for $(2\bar{2}0)_{Cu}$. In addition to decreasing the amount of Ti that is solidly dissolved in the Cu matrix, lowering lattice distortion of the Cu matrix, and improving the electrical conductivity of the alloy, the Cu$_4$Ti phase precipitation can reinforce the Cu-Ti-Zr alloy.

The Cu-Ti-Zr-La alloy's TEM microstructure after 30 min of aging at 450 °C is shown in Fig. 9. The bright-field images of the alloys in Fig. 9(a) and (b) show the formation of dislocation cells by dislocation entanglements, together with a multitude of nanoscale precipitated phases. The SAED iconography of Fig. 9(c) identifies it as a Cu matrix, which has a crystallo-

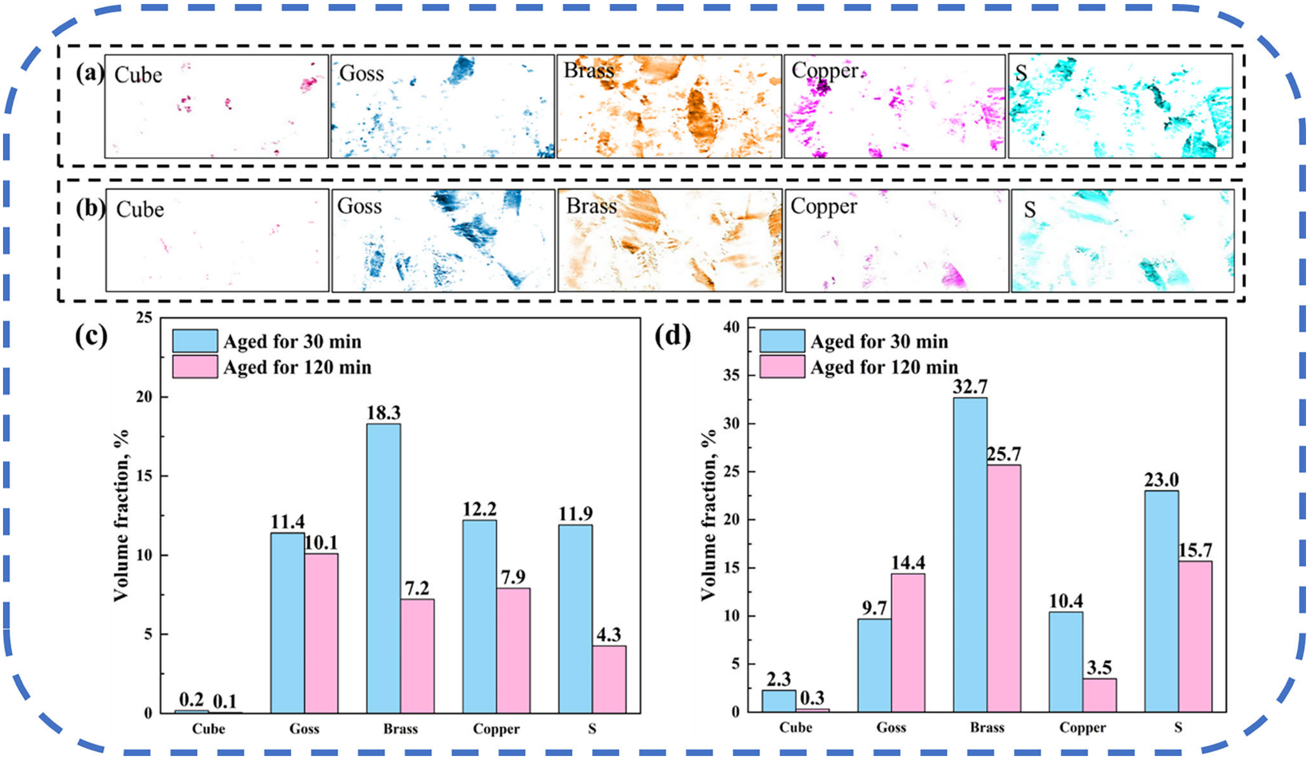

Fig. 7 Texture of Cu-Ti-Zr and Cu-Ti-Zr-La alloys aged at 450 °C: (a, b) Cu-Ti-Zr-La alloys aged for 30 min and 120 min, (c) Cu-Ti-Zr, (d) Cu-Ti-Zr-La alloys

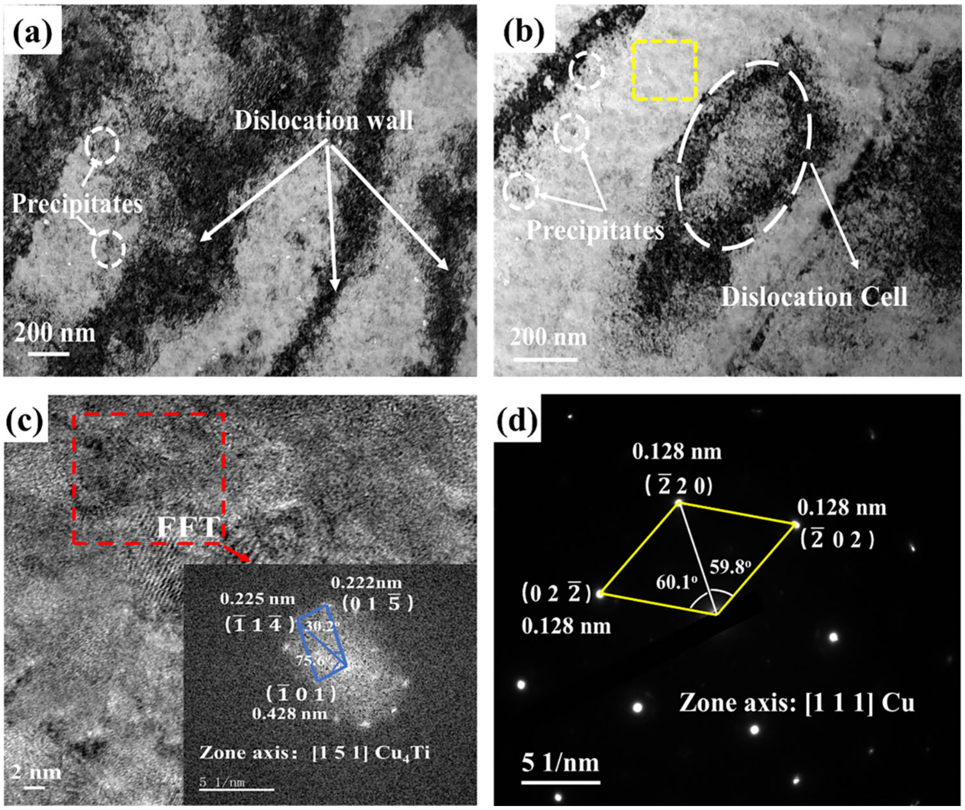

Fig. 8 TEM image of the Cu-Ti-Zr alloy aged at 450 °C for 30 min: (a) and (b) bright-field images, (c) HRTEM image of Cu_4Ti, (d) diffraction spots of the matrix

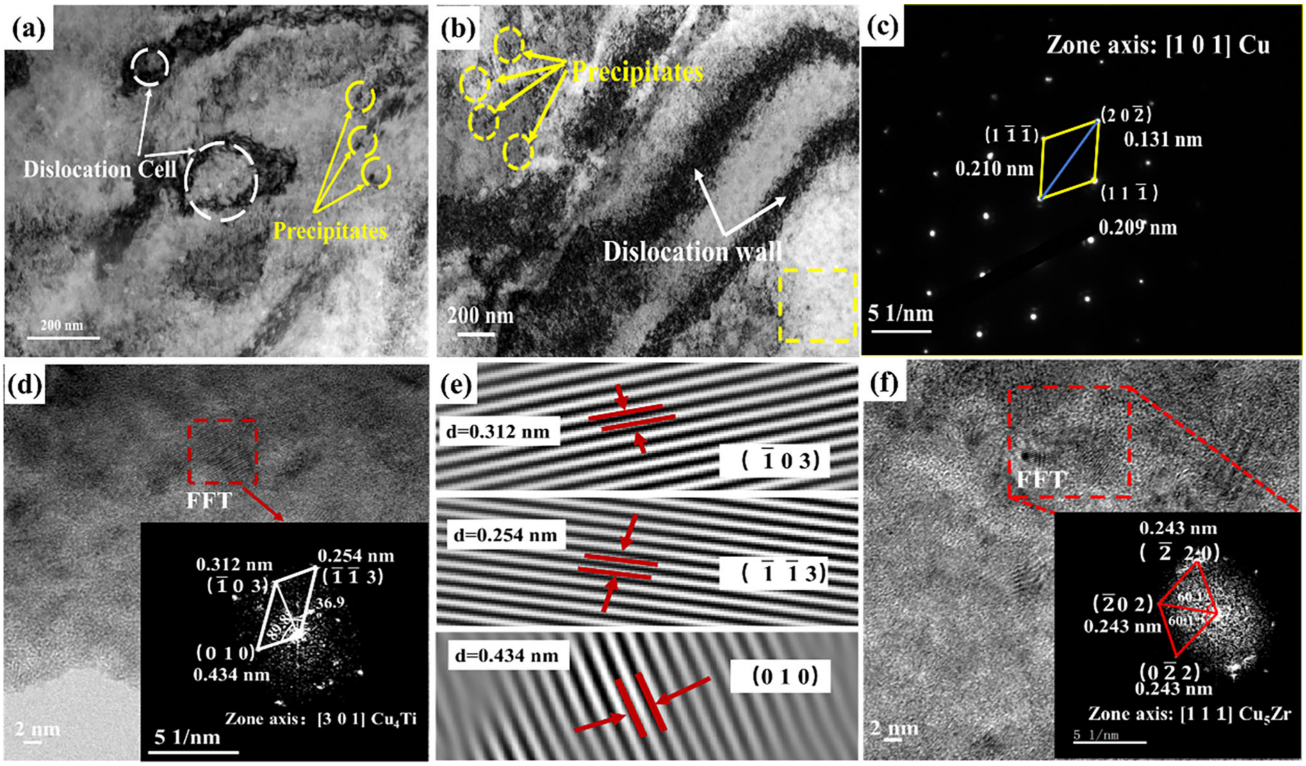

Fig. 9 TEM image of the Cu-Ti-Zr-La alloy aged at 450 °C for 30 min: (a) and (b) bright-field images, (c) SAED map of the Cu matrix, (d) HRTEM map of Cu_4Ti, (e) IFFT image of Cu_4Ti, (f) HRTEM map of Cu_5Zr

graphic axis of $[101]_{Cu}$, and the crystal spacing was measured to be 0.210 nm for $(1\ \overline{1}\overline{1})_{Cu}$, 0.131 nm for $(2\ 0\overline{2})_{Cu}$, and 0.209 nm for $(1\ 1\overline{1})_{Cu}$. In order to determine the type of precipitated phase of Cu-Ti-Zr-La alloy, HRTEM images were analyzed as shown in Fig. 9(d) and (f). By calibrating the diffraction spots obtained from the selected region of Fig. 9(d), the precipitated phase was found to be Cu_4Ti, and the crystallographic band axis of the nanoscale precipitated phase was calculated to be $[301]_{Cu4Ti}$. Figure 9(e) demonstrates the IFFT of the precipitated phase of Cu_4Ti, which yields a crystal spacing of 0.312 nm for $(\overline{1}03)_{Cu4Ti}$, 0.254 nm for $(\overline{1}\overline{1}3)_{Cu4Ti}$, and 0.434 nm for $(010)_{Cu4Ti}$. The FFT map was obtained by fast Fourier transformation of Fig. 9(f), and the diffraction spots were calibrated and determined to be the Cu_5Zr phase, which was measured to have a crystallographic spacing of 0.243 nm for $(\overline{2}20)_{Cu5Zr}$, 0.243 nm for $(0\overline{2}2)_{Cu5Zr}$, and 0.243 nm for $(\overline{2}02)_{Cu5Zr}$, giving its crystallographic axes of $[11\ 1]_{Cu5Zr}$. Cu-Ti-Zr-La alloy precipitates a large number of Cu_4Ti nanoprecipitated phases and Cu_5Zr precipitated phases during the aging process, and the precipitation strengthening effect makes the strength of the alloy increase. Moreover, the precipitation of solute atoms reduces lattice distortions in the matrix, which increases electrical conductivity.

By analyzing the TEM results of Cu-Ti-Zr and Cu-Ti-Zr-La alloys, it can be seen that both alloys precipitated Cu_4Ti phases during aging. However, the addition of the rare earth element La caused the precipitation of the Cu_5Zr phase in the Cu-Ti-Zr-La alloy during the aging process, realizing the complex phase reinforcement of Cu_4Ti and Cu_5Zr nanoprecipitated phases. This enhances the alloy's strength and hardness, as well as its overall mechanical properties.

4. Discussion

4.1 Strengthening Mechanisms of the Cu-Ti-Zr-La Alloy

Due to Zr, Ti, and La in Cu-Ti-Zr-La alloys, the Cu matrix atomic radius difference is large, as solid solution treatment caused lattice distortion, and 60% cold rolling resulted in aggregation of dislocations and entanglement of dislocations, the formation of dislocation walls and dislocation cells, further strengthening of the matrix. After aging treatment, the precipitated phases further strengthen the Cu matrix. Copper alloys are mainly strengthened by precipitation, cold deformation, fine grain, solution strengthening, and other ways. According to the mixing law, the strengthening increments of the alloys can be obtained by linear summation. Thus, the Cu-Ti-Zr-La alloy's strength (σ_y) can be computed as (Ref 44):

$$\sigma_y = \sigma_0 + \sigma_{ss} + \sigma_d + \sigma_{gb} + \sigma_p \qquad \text{(Eq 2)}$$

Here σ_0 is the frictional stress of the Cu-Ti-Zr alloy (simplified as the intrinsic frictional stress of oxygen-free Cu, which is about 52 MPa (Ref 45), σ_{ss} is the solution-strengthening increment, σ_d is the dislocation-strengthening increment, σ_p is the precipitation-strengthening increment, and σ_{gb} is the grain-boundary-strengthening increment.

(1) Solution Strengthening

Following the solid solution of the Cu-Ti-Zr-La alloy, a significant amount of Ti, Zr, La, and Cu atoms dissolve in the Cu matrix and atoms, respectively. The atomic size of the dissolved solute atoms is changed, which causes lattice distortions and produces solution strengthening effect. The difference in radii between the Cu, Ti, La, and Zr atoms is connected to the mechanism of strengthening in solid solutions. Solution strengthening of Cu-Ti-Zr-La alloys can be obtained from the Fleischer relation (Ref 46):

$$\sigma_{ss} = G\left(|\delta| + \frac{1}{20}\right)|\eta|^{\frac{3}{2}}\sqrt{\frac{x_a}{3}} \qquad \text{(Eq 3)}$$

Here G is the alloy's shear modulus (G = 46 GPa), δ is the alloy's lattice variation parameter (δ = 0.1105), and η is the alloy's shear modulus variation parameter (η = 0.3171), and x_a is the Cu-Ti-Zr alloy's solute atom mass percentage. (The contents of Ti, Zr, and La are 1.94%, 0.301%, and 0.213%, respectively.) Based on Eq. (3) yields, σ_{ss} = 119.2 MPa.

(2) Dislocation Strengthening

Solution treatment, 60% cold deformation, and cold rolling of the Cu-Ti-Zr-La alloy result in a significant amount of dislocations, which can fortify the copper matrix. After solution aging treatment, the alloy will precipitate a large number of phases, hindering the dislocation movement in the matrix. The Bailey–Hirsch formula can be used to determine how much dislocation density contributes to an alloy's yield strength (Ref 47):

$$\sigma_d = M\alpha Gb\rho^{\frac{1}{2}} \qquad \text{(Eq 4)}$$

Here M is the Taylor factor (M = 3.06), α is a constant (α = 0.3 in pure copper), G as above (G = 46 GPa), b is the Burgers vector (b = 0.2556 nm), and ρ is the alloy's dislocation density ($\rho = 2.58 \times 10^{14}$ m^{-2}). Calculation according to equation (3) gives σ_d=173.4 MPa.

(3) Grain Boundary Strengthening

As more precipitated phases are precipitated with aging, the overall area of grain boundaries grows, preventing dislocation movement and resulting in dislocation entanglement, which boosts the strength of Cu-Ti-Zr-La alloys. The Hall–Petch relationship can be used to calculate the strengthening of the grain boundaries (Ref 48):

$$\sigma_{gb} = \frac{K_y}{\sqrt{d}} \qquad \text{(Eq 5)}$$

Here K_y is the Hall–Petch constant (K_y=150 MPa $\mu m^{\frac{1}{2}}$) and d is the grain size (d = 30 μm). Consequently, the Cu-Ti-Zr-La alloy's grain boundary strengthening increment can be calculated as σ_{gb} = 27.4 MPa.

(4) Precipitation Strengthening

The most central issue in precipitation-strengthened alloys is the way in which the precipitated particles interact with dislocations. The precipitated phases of the Cu-Ti-Zr alloys interact with dislocations through a bypassing mechanism, called the Orowan mechanism. $\Delta\tau = Gb/L$ can be expressed as the hard particle strengthening relation proposed by Orowan (Ref 49). Here G and b as above, L is the precipitated phase particle spacing.

The relationship between the precipitation phase spacing and the yield strength is provided by $\Delta\tau = Gb/L$, however, the parameters affecting the precipitation phase strengthening are not entirely accurate. In recent years, with the in-depth study of precipitation-strengthened alloys, the Orowan strengthening has been further refined, and more parameters related to precipitation strengthening have been introduced:

$$\sigma_p = 0.81 \times \frac{MGb}{2\pi(1-\upsilon)^{\frac{1}{2}}} \times \frac{\ln\left(\frac{d_p}{b}\right)}{(\lambda - d_p)} \qquad \text{(Eq 6)}$$

$$\lambda = \frac{1}{2}d_p\sqrt{\frac{3\pi}{2f_p}} \qquad \text{(Eq 7)}$$

Here G and b as above, υ is Poisson's ratio (υ = 0.34), d_p is the precipitated grain size (d_p = 5.4 nm), λ is the crystallographic spacing between precipitated phases, and f_p is the precipitated phase's volume percentage (f_p = 1.8 %). Therefore, the calculation can be obtained σ_p = 460.7 MPa. Finally, the yield strength of Cu-Ti-Zr-La alloy can be obtained as $\sigma_y = \sigma_0 + \sigma_{ss} + \sigma_d + \sigma_{gb} + \sigma_p$=832.7 MPa, which is similar to the measured strength (824 MPa).

From the above analysis, the specific contributions of precipitation, cold deformation, grain boundary and solution strengthening mechanisms can be obtained, shown in Fig. 10. Because the precipitated phases have a strengthening effect that leads to higher properties with aging, the precipitation strengthening is stronger (460.7 MPa).

5. Conclusions

By subjecting Cu-Ti-Zr and Cu-Ti-Zr-La alloys to solution treatment at 900 °C for 1 h, 60% rolling deformation, and aging treatments, after analysis of the evolution of the organization and properties of alloys during deformation heat treatment and strengthening mechanisms, the following conclusions were reached:

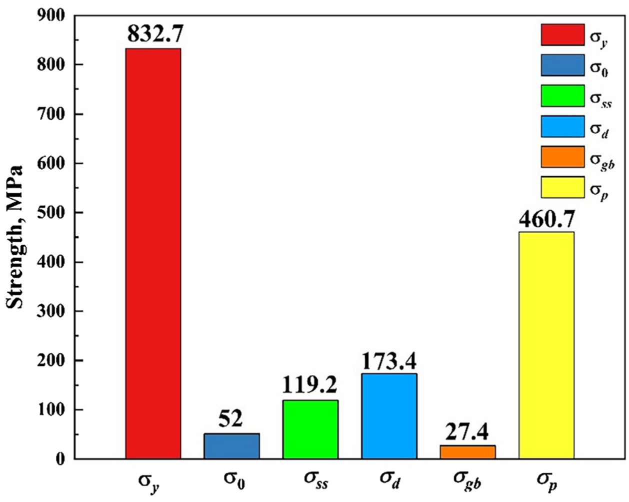

Fig. 10 Strength distribution histogram of the Cu-Ti-Zr-La alloys

(1) For the Cu-Ti-Zr and Cu-Ti-Zr-La alloys, aging at 450 °C for 30 min is the optimum process parameter. In these circumstances, the Cu-Ti-Zr-La has a microhardness of 295 HV and a tensile strength of 824 MPa. The Cu-Ti-Zr-La alloy showed an increase in microhardness and strength by 8.5% and 5%, respectively, compared to the Cu-Ti-Zr alloy.

(2) The EBSD characterization of the two alloys after aging showed that the addition of rare earth element La inhibited the grain growth, the grain refinement was more obvious, the content of Brass texture, S texture and Cube texture was higher, and the fine grain strengthening effect made the Cu-Ti-Zr-La alloy have higher strength.

(3) TEM analysis shows that Cu_4Ti nanophase is precipitated in both alloys during aging, and Cu_5Zr phase is found in Cu-Ti-Zr-La alloy.

(4) By calculating and analyzing the strengthening mechanism of Cu-Ti-Zr-La alloy, it is found that precipitation strengthening contributes the most to the strength.

Acknowledgments

This work was supported by the National Natural Science Foundation of China (52071134), the Joint Foundation for Science and Technology Research and Development Plan of Henan Province (232103810030, 232103810031), the Program for Innovative Research Team at the University of the Henan Province (22IRTSTHN001), the China Postdoctoral Science Foundation (2023TQ0107), Key Research and Development Program of the Jiangxi Province (20224BBE52002).

References

1. Q. Lei, Z. Xiao, W. Hu, B. Derby, and Z. Li, Phase Transformation Behaviors and Properties of a High Strength Cu-Ni-Si Alloy, *Mater. Sci. Eng. A*, 2017, **697**, p 37–47. https://doi.org/10.1016/j.msea.2017.05.001
2. K.X. Song, Y.F. Geng, Y.J. Ban, Y. Zhang, Z. Li, X.J. Mi, J. Cao, Y.J. Zhou, and X.B. Zhang, Effect of Strain Rates on Dynamic Deformation Behavior of Cu-20Ag Alloy, *J. Mater. Res. Technol.*, 2021, **79**, p 75–87. https://doi.org/10.1016/j.jmst.2020.11.043
3. Y. Zhang, H.L. Sun, A.A. Volinsky, B.H. Tian, K.X. Song, B.J. Wang, and Y. Liu, Hot Workability and Constitutive Model of the Cu-Zr-Nd Alloy, *Vacuum*, 2017, **146**, p 35–43. https://doi.org/10.1016/j.vacuum.2017.09.017
4. R. Mishnev, I. Shakhova, A. Belyakov, and R. Kaibyshev, Deformation Microstructures, Strengthening Mechanisms, and Electrical Conductivity in a Cu-Cr-Zr Alloy, *Mater. Sci. Eng. A*, 2015, **629**, p 29–40. https://doi.org/10.1016/j.msea.2015.01.065
5. S.L. Tang, M. Zhou, X. Li, Y. Zhang, D.Y. Xu, Z.Y. Zhang, B.H. Tian, Y.L. Jia, Y. Liu, A.A. Volinsky, and E.S. Marchenko, Microstructure and Hot Deformation Behavior of the Cu-1Ni-0.9Sn-0.5Ti-0.3Cr Alloy, *Mater. Today Commun.*, 2022, **31**, p 103771. https://doi.org/10.1016/j.mtcomm.2022.103771
6. Y.F. Geng, X. Li, Y. Zhang, Y.L. Jia, H.L. Zhou, B.H. Tian, Y. Liu, A.A. Volinsky, X.H. Zhang, K.X. Song, P. Liu, and X.H. Chen, Microstructure Evolution of Cu-1.0Co-0.65Si-0.1Ti Alloy During Hot Deformation, *Vacuum*, 2020, **177**, p 109376. https://doi.org/10.1016/j.vacuum.2020.109376
7. A. Meng, J.F. Nie, K. Wei, H.J. Kang, Z.J. Liu, and Y.H. Zhao, Optimization of Strength, Ductility and Electrical Conductivity of a Cu-Cr-Zr Alloy by Cold Rolling and Aging Treatment, *Vacuum*, 2019, **167**, p 329–335. https://doi.org/10.1016/j.vacuum.2019.06.027
8. W. Wang, H.J. Kang, Z.N. Chen, Z.J. Chen, C.L. Zou, R.G. Li, G.M. Yin, and T.M. Wang, Effects of Cr and Zr Additions on Microstructure and Properties of Cu-Ni-Si Alloys, *Mater. Sci. Eng. A*, 2016, **673**, p 378–390. https://doi.org/10.1016/j.msea.2016.07.021
9. J. Chalon, J.D. Guérin, L. Dubar, A. Dubois, and E.S. Puchi-Cabrera, Characterization of the Hot-Working Behavior of a Cu-Ni-Si Alloy, *Mater. Sci. Eng. A*, 2016, **667**, p 77–86. https://doi.org/10.1016/j.msea.2016.04.061
10. Y.C. Tang, Y.L. Kang, L.J. Yue, and X.L. Jiao, Mechanical Properties Optimization of a Cu-Be-Co-Ni Alloy by Precipitation Design, *J. Alloys Compd.*, 2017, **695**, p 613–625. https://doi.org/10.1016/j.jallcom.2016.11.014
11. Y.C. Tang, Y.L. Kang, L.J. Yue, and X.L. Jiao, The Effect of Aging Process on the Microstructure and Mechanical Properties of a Cu-Be-Co-Ni Alloy, *Mater. Des.*, 2015, **85**, p 332–341. https://doi.org/10.1016/j.matdes.2015.06.157
12. Y.C. Tang, G.M. Zhu, Y.L. Kang, L.J. Yue, and X.L. Jiao, Effect of Microstructure on the Fatigue Crack Growth Behavior of Cu-Be-Co-Ni Alloy, *J. Alloys Compd.*, 2016, **663**, p 784–795. https://doi.org/10.1016/j.jallcom.2015.12.017
13. S. Nagarjuna, U.C. Babu, and P. Ghosal, Effect of Cryo-Rolling on Age Hardening of Cu-1.5 Ti Alloy, *Mater. Sci. Eng. A*, 2008, **491**, p 331–337. https://doi.org/10.1016/j.msea.2008.02.014
14. F.L. Wang, Y.P. Li, K. Wakoh, Y. Koizumi, and A. Chiba, Cu-Ti-C Alloy with High Strength and High Electrical Conductivity Prepared by Two-Step Ball-Milling Processes, *Mater. Des.*, 2014, **61**, p 70–74. https://doi.org/10.1016/j.matdes.2014.04.034
15. C. Li, X.H. Wang, B. Li, J. Shi, Y.F. Liu, and P. Xiao, Effect of Cold Rolling and Aging Treatment on the Microstructure and Properties of Cu-3Ti-2Mg Alloy, *J. Alloys Compd.*, 2020, **818**, p 152915. https://doi.org/10.1016/j.jallcom.2019.152915
16. X. Wang, Z. Xiao, W.T. Qiu, Z. Li, and F. Liu, The Evolution of Microstructure and Properties of a Cu-Ti-Cr-Mg-Si Alloy with High Strength During the Multi-Stage Thermomechanical Treatment, *Mater. Sci. Eng. A*, 2021, **803**, p 140510. https://doi.org/10.1016/j.msea.2020.140510
17. L. Huang, L.J. Peng, X.J. Mi, G. Zhao, G.J. Huang, H.F. Xie, and W.J. Zhang, Relationship Between Microstructure and Properties of High-Strength Cu-Ti-Cr Alloys During Aging, *J. Alloys Compd.*, 2023, **942**, p 168865. https://doi.org/10.1016/j.jallcom.2023.168865
18. W. Huan, X.Y. Dai, P.J. Han, C.Z. Zhou, Y.H. Wei, and L.F. Hou, Age Hardening Studies of a Cu-4Ti-Cr-Fe Alloy, *Mater. Sci. Technol.*, 2019, **35**, p 1848–1855. https://doi.org/10.1080/02670836.2019.1651474
19. L. Rong, Z. Xiao, Z. Li, X.P. Meng, and X. Wang, Work Hardening Behavior and Microstructure Evolution of a Cu-Ti-Cr-Mg Alloy During Room Temperature and Cryogenic Rolling, *Materials*, 2023, **16**, p 424. https://doi.org/10.3390/ma16010424
20. X. Wang, Z. Li, Z. Xiao, and W.T. Qiu, Microstructure Evolution and Hot Deformation Behavior of Cu-3Ti-0.1Zr Alloy with Ultra-High Strength, *Trans. Nonferrous Met. Soc. China*, 2020, **30**, p 2737–2748. https://doi.org/10.1016/S1003-6326(20)65416-4
21. H. Doi, S. Suzuki, K. Mimura, M. Isshiki, and Y. Waseda, Electrical Conductivity and Hardness of Quenched and Aged High-Purity Cu-Ti-Al Alloys, *J. Jpn. I. Met.*, 2004, **68**, p 78–81. https://doi.org/10.2320/jinstmet.68.78
22. W.J. Liu, J. Li, X. Chen, M.H. Ji, X.P. Xiao, H. Wang, and B. Yang, Effect of Vanadium on the Microstructure and Kinetics of Discontinuous Precipitation in Cu-3.2Ti-0.2Fe Alloy, *J. Mater. Res. Technol.*, 2021, **14**, p 121–136. https://doi.org/10.1016/j.jmrt.2021.06.045
23. I.S. Batra, A. Laik, G.B. Kale, G.K. Dey, and U.D. Kulkarni, Microstructure and Properties of a Cu-Ti-Co Alloy, *Mater. Sci. Eng. A*, 2005, **402**, p 118–125. https://doi.org/10.1016/j.msea.2005.04.015
24. S.F. Fang, Prediction of the Hardness of Cu-Ti-Co Alloy Using Machine Learning Techniques, *Key Eng. Mater.*, 2018, **777**, p 372–376. https://doi.org/10.4028/www.scientific.net/KEM.777.372
25. S. Nagarjuna, K.K. Sharma, I. Sudhakar, and D.S. Sarma, Age Hardening Studies in a Cu-4.5 Ti-0.5 Co Alloy, *Mater. Sci. Eng. A*, 2001, **313**, p 251–260. https://doi.org/10.1016/S0921-5093(00)01834-7
26. R. Markandeya, S. Nagarjuna, and D.S. Sarma, Effect of Prior Cold Work on Age Hardening of Cu-4Ti-1Cr Alloy, *Mater. Sci. Eng. A*, 2005, **404**(1–2), p 305–313. https://doi.org/10.1016/j.msea.2005.05.072

27. R. Markandeya, S. Nagarjuna, and D.S. Sarma, Effect of Prior Cold Work on Age Hardening of Cu-3Ti-1Cr Alloy, *Mater. Char.*, 2006, **57**(4–5), p 348–357. https://doi.org/10.1016/j.matchar.2006.02.017
28. R. Markandeya, S. Nagarjuna, and D.S. Sarma, Precipitation Hardening of Cu-Ti-Cr Alloys, *Mater. Sci. Eng. A*, 2004, **371**(1–2), p 291–305. https://doi.org/10.1016/j.msea.2003.12.002
29. T.J. Konno, R. Nishio, S. Semboshi, T. Ohsuna, and E. Okunishi, Aging Behavior of Cu-Ti-Al Alloy Observed by Transmission Electron Microscopy, *J. Mater. Sci.*, 2008, **43**, p 3761–3768. https://doi.org/10.1007/s10853-007-2233-2
30. X.H. Wang, C.Y. Chen, T.T. Guo, J.T. Zou, and X.H. Yang, Microstructure and Properties of Ternary Cu-Ti-Sn Alloy, *J. Mater. Eng. Perform.*, 2015, **24**, p 2738–2743. https://doi.org/10.1007/s11665-015-1483-4
31. X.M. Cao, H.Q. Li, C.J. Xiang, C.X. Yang, and F.A. Guo, Effect of Zr on heat-resistance of Cu-Ti alloy, *Hot Working Technol.*, 2008, **14**, p 16–18. https://doi.org/10.14158/j.cnki.1001-3814.2008.14.005
32. R. Markandeya, S. Nagarjuna, and D.S. Sarma, Influence of Prior Cold Work on Age Hardening of Cu-Ti-Zr Alloys, *Mater. Sci. Technol.*, 2005, **21**(10), p 1171–1180. https://doi.org/10.1179/174328405X58922
33. S.L. Tang, M. Zhou, Y. Zhang, D.Y. Xu, Z.Y. Zhang, X.H. Zheng, D. Li, X. Li, B.H. Tian, Y.L. Jia, Y. Liu, A.A. Volinsky, and E.S. Marchenko, Improved Microstructure, Mechanical Properties and Electrical Conductivity of the Cu-Ni-Sn-Ti-Cr Alloy Due to Ce Micro-Addition, *Mater. Sci. Eng. A*, 2023, **871**, p 144910. https://doi.org/10.1016/j.msea.2023.144910
34. Z.Y. Zhang, M. Zhou, Y. Zhang, S.L. Tang, D.Y. Xu, B.H. Tian, X. Li, Y.L. Jia, Y. Liu, and A.A. Volinsky, Ce Effects on Deformation-Induced Microstructure Evolution in Cu-Ti-Ni-Mg Alloys, *Adv. Eng. Mater.*, 2023, **25**, p 2201913. https://doi.org/10.1002/adem.202201913
35. H. Li, P. Chen, Z.X. Wang, F. Zhu, R.G. Song, and Z.Q. Zheng, Tensile Properties, Microstructures and Fracture Behaviors of an Al-Zn-Mg-Cu Alloy During Ageing After Solution Treating and Cold-Rolling, *Mater. Sci. Eng. A*, 2019, **742**, p 798–812. https://doi.org/10.1016/j.msea.2018.03.098
36. Y.K. Xie, Y.L. Deng, Y. Wang, and X.B. Guo, Effect of Asymmetric Rolling and Subsequent Ageing on the Microstructure, Texture and Mechanical Properties of the Al-Cu-Li Alloy, *J. Alloys Compd.*, 2020, **836**, p 155445. https://doi.org/10.1016/j.jallcom.2020.155445
37. S.L. Fu, P. Liu, X.H. Chen, H.L. Zhou, F.C. Ma, W. Li, and K. Zhang, Effect of Aging Process on the Microstructure and Properties of Cu-Cr-Ti Alloy, *Mater. Sci. Eng. A*, 2021, **802**, p 140598. https://doi.org/10.1016/j.msea.2020.140598
38. D.R. Curran, L. Seaman, and D.A. Shockey, Dynamic Failure of Solids, *Phys. Rep.*, 1987, **147**(5–6), p 253–388. https://doi.org/10.1016/0370-1573(87)90049-4
39. C. Li, H. Tan, W.M. Wu, S. Zhao, and H.B. Zhang, Effect of Electropulsing Treatment on Microstructure and Tensile Fracture Behavior of Nanocrystalline Ni Foil, *Mater. Sci. Eng. A*, 2016, **657**, p 347–352. https://doi.org/10.1016/j.msea.2016.01.075
40. J.W. Li, J. Xu, B. Guo, D.B. Shan, and T.G. Langdon, Shear Fracture Mechanism in Micro-Tension of an Ultrafine-Grained Pure Copper Using Synchrotron Radiation X-ray Tomography, *Scr. Mater.*, 2017, **132**, p 25–29. https://doi.org/10.1016/j.scriptamat.2017.01.021
41. D. Jorge-Badiola, A. Iza-Mendia, and I. Gutiérrez, Study by EBSD of the Development of the Substructure in a Hot Deformed 304 Stainless Steel, *Mater. Sci. Eng. A*, 2005, **394**(1–2), p 445–454. https://doi.org/10.1016/j.msea.2004.11.049
42. C. Haase, and L.A. Barrales-Mora, Influence of Deformation and Annealing Twinning on the Microstructure and Texture Evolution of Face-Centered Cubic High Entropy Alloys, *Acta Mater.*, 2018, **150**, p 88–103. https://doi.org/10.1016/j.actamat.2018.02.048
43. Y.F. Geng, Y.J. Ban, X. Li, Y. Zhang, Y.L. Jia, B.H. Tian, M. Zhou, Y. Liu, A.A. Volinsky, K.X. Song, and S.L. Tang, Excellent Mechanical Properties and High Electrical Conductivity of Cu-Co-Si-Ti Alloy Due to Multiple Strengthening, *Mater. Sci. Eng. A*, 2021, **821**, p 141639. https://doi.org/10.1016/j.msea.2021.141639
44. H.M. Wen, T.D. Topping, D. Isheim, D.N. Seidman, and E.J. Lavernia, Strengthening Mechanisms in a High-Strength Bulk Nanostructured Cu-Zn-Al Alloy Processed via Cryomilling and Spark Plasma Sintering, *Acta Mater.*, 2013, **61**(8), p 2769–2782. https://doi.org/10.1016/j.actamat.2012.09.036
45. X.W. Zuo, K. Han, C.C. Zhao, R.M. Niu, and E.G. Wang, Microstructure and Properties of Nanostructured Cu-28wt%Ag Microcomposite Deformed After Solidifying Under a High Magnetic Field, *Mater. Sci. Eng. A*, 2014, **619**, p 319–327. https://doi.org/10.1016/j.msea.2014.09.070
46. J. Freudenberger, J. Lyubimova, A. Gaganov, H. Witte, A.L. Hickman, H. Jones, and M. Nganbe, Non-destructive Pulsed Field Cu Ag-Solenoids, *Mater. Sci. Eng. A*, 2010, **527**(7–8), p 2004–2013. https://doi.org/10.1016/j.msea.2009.11.038
47. S.C. Wang, Z. Zhu, and M.J. Starink, Estimation of Dislocation Densities in Cold Rolled Al-Mg-Cu-Mn Alloys by Combination of Yield Strength Data, EBSD and Strength Models, *J. Microsc.*, 2005, **217**, p 174–178. https://doi.org/10.1111/j.1365-2818.2005.01449.x
48. Y. Liu, Z. Li, Y.X. Jiang, Y. Zhang, Z.Y. Zhou, and Q. Lei, The Microstructure Evolution and Properties of a Cu-Cr-Ag Alloy During Thermal-Mechanical Treatment, *J. Mater. Res.*, 2017, **32**(7), p 1324–1332. https://doi.org/10.1557/jmr.2017.17
49. Y.K. Wu, Y. Li, J.Y. Lu, S. Tan, F. Jiang, and J. Sun, Correlations Between Microstructures and Properties of Cu-Ni-Si-Cr Alloy, *Mater. Sci. Eng.*, 2018, **731**, p 403–412. https://doi.org/10.1016/j.msea.2018.06.075